Article

Influence of Different Capping Agents on the Structural, Optical, and Photocatalytic Degradation Efficiency of Magnetite (Fe$_3$O$_4$) Nanoparticles

Thandi B. Mbuyazi and Peter A. Ajibade *

School of Chemistry and Physics, University of KwaZulu-Natal, Private Bag X01, Scottsville, Pietermaritzburg 3209, South Africa; 216006335@stu.ukzn.ac.za

* Correspondence: ajibadep@ukzn.ac.za

Abstract: Octylamine (OTA), 1-dodecanethiol (DDT), and tri-n-octylphosphine (TOP) capped magnetite nanoparticles were prepared by co-precipitation method. Powder X-ray diffraction patterns confirmed inverse spinel crystalline phases for the as-prepared iron oxide nanoparticles. Transmission electron microscopic micrographs showed iron oxide nanoparticles with mean particle sizes of 2.1 nm for Fe$_3$O$_4$-OTA, 5.0 nm for Fe$_3$O$_4$-DDT, and 4.4 nm for Fe$_3$O$_4$-TOP. The energy bandgap of the iron oxide nanoparticles ranges from 2.25 eV to 2.76 eV. The iron oxide nanoparticles were used as photocatalysts for the degradation of methylene blue with an efficiency of 55.5%, 58.3%, and 66.7% for Fe$_3$O$_4$-OTA, Fe$_3$O$_4$-DDT, and Fe$_3$O$_4$-TOP, respectively, while for methyl orange the degradation efficiencies were 63.8%, 47.7%, and 74.1%, respectively. The results showed that tri-n-octylphosphine capped iron oxide nanoparticles are the most efficient iron oxide nano-photocatalysts for the degradation of both dyes. Scavenger studies show that electrons (e$^-$) and hydroxy radicals (•OH) contribute significantly to the photocatalytic degradation reaction of both methylene blue and methyl orange using Fe$_3$O$_4$-TOP nanoparticles. The influence of the dye solution's pH on the photocatalytic reaction reveals that a pH of 10 is the optimum for methylene blue degradation, whereas a pH of 2 is best for methyl orange photocatalytic degradation using the as-prepared iron oxide nano-photocatalyst. Recyclability studies revealed that the iron oxide photocatalysts can be recycled three times without losing their photocatalytic activity.

Keywords: iron oxide; nanoparticle; photocatalytic degradation; methylene blue; methyl orange

1. Introduction

Water contamination is currently a life-threatening issue and public health emergency that must be addressed promptly to improve global water quality and maintain a healthy ecosystem [1,2]. The excessive discharge of environmental contaminants like organic dyes has become a hinderance to the provision of potable water worldwide [3–5]. Organic dyes, with their complex chemical structures with high molecular weights, degrade slowly, are presumably mutagenic and carcinogenic, and have the capacity to block light penetration, hence reducing photosynthetic reactions. As a result, dye-containing effluents disrupt the natural balance of the surface water and significantly impact human health and aquatic ecosystems [6–9].

Magnetic metal oxide nanoparticles such as ZnO [10,11], CuO [12,13], SnO$_2$ [14], TiO$_2$ [15,16], MgO, and FeO [17,18] have been used as photocatalysts to degrade organic dyes and as adsorbents for removing heavy metal ions. Magnetic photocatalysts combine catalytic characteristics with magnetism, allowing the photocatalyst to be conveniently recovered from the treated solution using an external magnetic field. Magnetic iron oxide nanoparticles, among other forms of nanomaterials, offer unique properties such as abundance, good resistance to corrosion, low toxicity, and chemical and photochemical

stability, making them an attractive material for photocatalysis [19–22]. However, magnetic iron oxide nanoparticles have high surface energies because of their high specific surface-to-volume ratios; therefore, they tend to aggregate to reduce the surface energy, which can change their adsorption ability and magnetic efficiency [23]. Consequently, it is critical to control the particle sizes and distributions of magnetic nanomaterials to prevent agglomeration.

Surfactant selection is of paramount importance in the preparation of magnetic nanoparticles to prevent their aggregation and create narrow particle size distributions with optimal shape and morphology. Numerous studies on the passivation of iron oxide nanoparticles using capping agents have been conducted. Sodipo et al. [24] studied the influence of five different capping agents on the morphology and magnetic properties of magnetite nanoparticles. Sodium citrate was the most effective capping agent, producing nearly spherical nanoparticles with the least agglomeration. Sharma et al. [25] prepared α-Fe_2O_3 nanoparticles using sodium citrate, polyvinyl pyrrolidone (PVP), and starch as capping agents. The incorporation of capping agents into nanoparticles has been shown to improve their activity and stability as photocatalysts against methylene blue with a maximum efficiency of 98.8% dye removal using PVP-capped α-Fe_2O_3.

Guidolin et al. [26] prepared Fe_3O_4 nanoparticles by a sol–gel citrate–nitrate method. The magnetite nanoparticles degraded 93.4% of methylene blue after 210 min when $2250\ mg\cdot L^{-1}$ of the nanoparticles was used. Rivera et al. [27] investigated the Fenton-like process for methylene blue dye degradation utilizing Fe_3O_4 nanoparticles prepared by the electrochemical synthesis method. The results showed that complete degradation can be achieved using $2\ g\cdot L^{-1}$ of Fe_3O_4 nanoparticles at a concentration of 100 mg/L MB in an acidic medium. Modrogan et al. [28] evaluated the photocatalytic performance of the Fe_3O_4/PVA composite against methyl orange in the presence of hydrogen peroxide under UV light. Various reaction parameters, such as composite dosage, pH, and the amount of hydrogen peroxide (H_2O_2), were studied. The results indicated that the level of dye degradation is significantly dependent on the amount of H_2O_2 in the reaction medium. León-Flores et al. [29] reported the green synthesis of Fe_3O_4 nanoparticles, using the *Coffea arabica* L. extract to degrade methyl orange dye under UV light irradiation, and that 80% of the dye was degraded using 10 mg of the nanoparticles in 15 mL of dye solution. Moreover, studies have shown that the morphology and phase composition of iron oxide nanoparticles influences their photocatalytic efficiency [30].

In this study, we report the structural and optical studies of octylamine (OTA), 1-dodecanethiol (DDT), and tri-n-octylphosphine (TOP) capped iron oxide nanoparticles. The as-prepared iron oxide nanoparticles' potentials as photocatalysts were evaluated for the degradation of methylene blue and methyl orange dyes under visible light irradiation. The photodegradation kinetics, the influence of pH, scavengers, and photostability were also evaluated.

2. Materials and Methods

2.1. Materials

$FeCl_2\cdot 4H_2O$, $Fe_2(SO_4)_3\cdot H_2O$, 25% ammonia solution, ethanol, octylamine, 1-dodecanethiol, trioctylphosphine, methylene blue, methyl orange, ethylenediamine tetraacetic acid disodium, ascorbic acid, silver nitrate, isopropanol, hydrochloric acid, and sodium hydroxide were purchased from Merck (Darmstadt, Germany). All the reagents were used as purchased without further purification.

2.2. Synthesis of Iron Oxide Nanoparticles

Iron oxide nanoparticles were prepared using the co-precipitation approach [31]. The experiment was conducted in a nitrogen flow. $FeCl_2\cdot 4H_2O$ (0.2485 g, 0.00125 mol) and $Fe_2(SO_4)_3\cdot H_2O$ (1.0445 g, 0.0025 mol) were dissolved in 100 mL of distilled water and heated to 80 °C. An amount of 15 mL of 25% ammonia solution was added to adjust the pH of the reaction mixture to 11. After 30 min, octylamine (OTA) was introduced, and

the temperature was maintained at 80 °C and the reaction was further stirred for 1 h. The nanoparticles were then centrifuged at 3500 rpm and washed several times to remove the excess capping agent and unreacted materials. To evaluate the effect of capping agents, the same procedure was carried out with trioctylphosphine (TOP) and 1-dodecathiol (DDT).

2.3. Characterization

FTIR spectra were recorded using a Cary 630 FTIR spectrometer, and absorption spectra were recorded using a Perkin Elmer lambda 25 UV-Vis spectrophotometer. The dye degradation experiments were conducted using a 70W high-pressure mercury lamp. The morphology of the nanoparticles was determined using a transmission electron microscopy (TEM) image taken with a Japan Electrical Optical Laboratories (JEOL) JEM-1400 electron microscope equipped with Gatan digital microgram software. ImageJ analysis software was used to measure the particle size distribution.

2.4. Adsorption of Methylene Blue (MB) and Methyl Orange (MO) by Iron Oxide Nanoparticles

The batch adsorption efficiency of Fe_3O_4 nanoparticles was measured using methylene blue (MB) and methyl orange (MO) as model dyes. Typically, 50 mg of Fe_3O_4 nanoparticles were dispersed in 40 mL of 10 mg/L of dye solution and the mixture was stirred in the dark for 75 min. An aliquot was withdrawn from each flask at 15 min time intervals and was analyzed with a UV-visible spectrometer to determine dye removal. The adsorption capacity, Q (mg/g), of the adsorbent was calculated using Equation (1):

$$Q = \left(\frac{C_0 - C_t}{W} \right) V \tag{1}$$

where C_0 is the initial concentration of dye (mg L^{-1}), C_t is the concentration of dye (mg L^{-1}) in solution at a time 't', V is the volume (L) of the dye solution, and W is the mass (g) of the adsorbent used.

2.5. Photocatalytic Experiment

Methylene blue (MB) and methyl orange (MO) dyes were used to investigate the dye degradation performance of iron oxide nanoparticles. In a typical method, a stock solution is prepared by dissolving 10 mg each of MB and MO in 1000 mL of distilled water. A total of 40 mg of iron oxide nanoparticles were dispersed in 40 mL of dye solution, sonicated for 60 min, and stirred in the dark for 60 min. The mixture was then irradiated with visible light and the photocatalytic degradation of the dye was evaluated using 4 mL of each mixed solution every 30 min. A UV-Vis spectrophotometer was used to evaluate the reaction progress by observing the absorbance maxima of the dyes. The degradation efficiency was calculated as:

$$D = \frac{A_0 - A_t}{A_0} \times 100 \tag{2}$$

where 'D' denotes degradation efficiency (%), A_0 refers to dye solution absorbance at 't' zero, and A_t to dye solution absorbance after time 't'.

2.6. Effect of pH

The influence of pH on the degradation efficiency of MB and MO under visible light was examined over a pH range of 2 to 10. The pH of the dye solutions was changed using 0.1 M aqueous HCl and NaOH solutions.

### 2.7. Radical Scavenger Experiment

To identify the primary reactive species generated during the photocatalytic degradation of MB and MO, scavenging studies were conducted. To do this, isopropanol (IPA), ethylenediamine tetraacetic acid disodium (EDTA-Na_2), ascorbic acid (AA), and silver nitrate (SN) were introduced to the reaction mixture to quench •OH, h^+, •O_2^-, and e^-, respectively. Then, 40 mg of the photocatalyst and 5 mL of each scavenger (10 mM) were

added to 40 mL of dye solution (10 ppm) [32]. The experiment was carried out for 180 min under visible light and the respective absorbance spectra were taken to monitor the reaction progress.

3. Results

3.1. Structural and Morphological Studies of the Iron Oxide Nanoparticles

Powder X-ray diffraction patterns of the as-prepared iron oxide nanoparticles are shown in Figure 1. All diffraction patterns were indexed to the single crystalline inverse spinel structure of magnetite with card No. 19-0629 [33,34]. The 2θ peaks are 21.45°, 35.30°, 41.59°, 50.67°, 63.14°, 67.68°, and 74.55°, corresponding to the (111), (220), (311), (400), (422), (511) and (440) planes of the cubic inverse spinel structure of Fe_3O_4. The crystal growth orientation preference is toward the (311) plane. The peaks are broad and well-defined which could be due to the small particle sizes and the crystalline nature of the as-prepared iron oxide nanoparticles. No other peaks corresponding to other phases were identified in the XRD patterns, indicating the formation of a pure Fe_3O_4 phase regardless of the capping agent used to prepare the iron oxide nanoparticles.
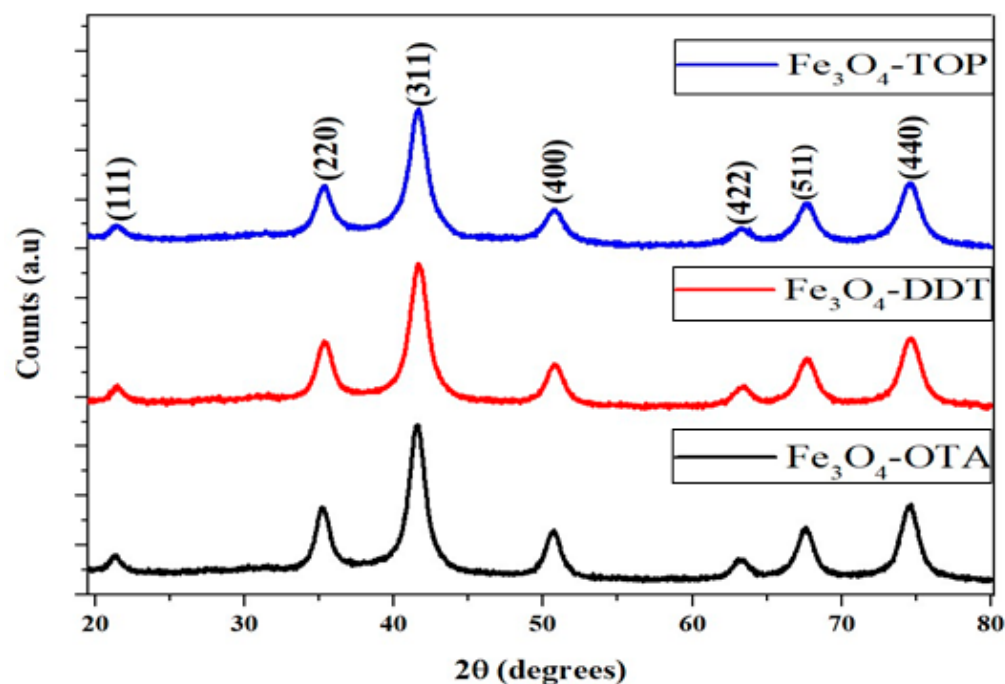
Figure 1. P-XRD diffraction patterns of OTA, DDT, and TOP-capped Fe_3O_4 nanoparticles.

TEM micrographs of the as-prepared iron oxide nanoparticles are shown in Figure 2. The TEM image of the OTA-capped iron oxide nanoparticles shows a mixture of square-like, oval, and quasi-spherical particles with an average size of 2.1 nm. The DDT-capped iron oxide nanoparticles also show agglomerated quasi-spherical particles with a mean particle size of 5.0 nm. The iron oxide nanoparticles prepared from TOP are also agglomerated with irregular shaped particles with a mean size of 4.4 nm (Figure S1). The observed agglomeration of the as-prepared nanoparticles may be attributed to the fact that they aggregate to reduce their high surface energy or to the dipole–dipole interactions of magnetic nanoparticles [24,35]. The use of capping agents resulted in more dispersed and well-defined shapes of nanoparticles compared to uncapped nanoparticles (Figure S2). Additionally, the use of different capping agents is observed to influence the as-prepared iron oxide nanoparticle sizes and shapes.
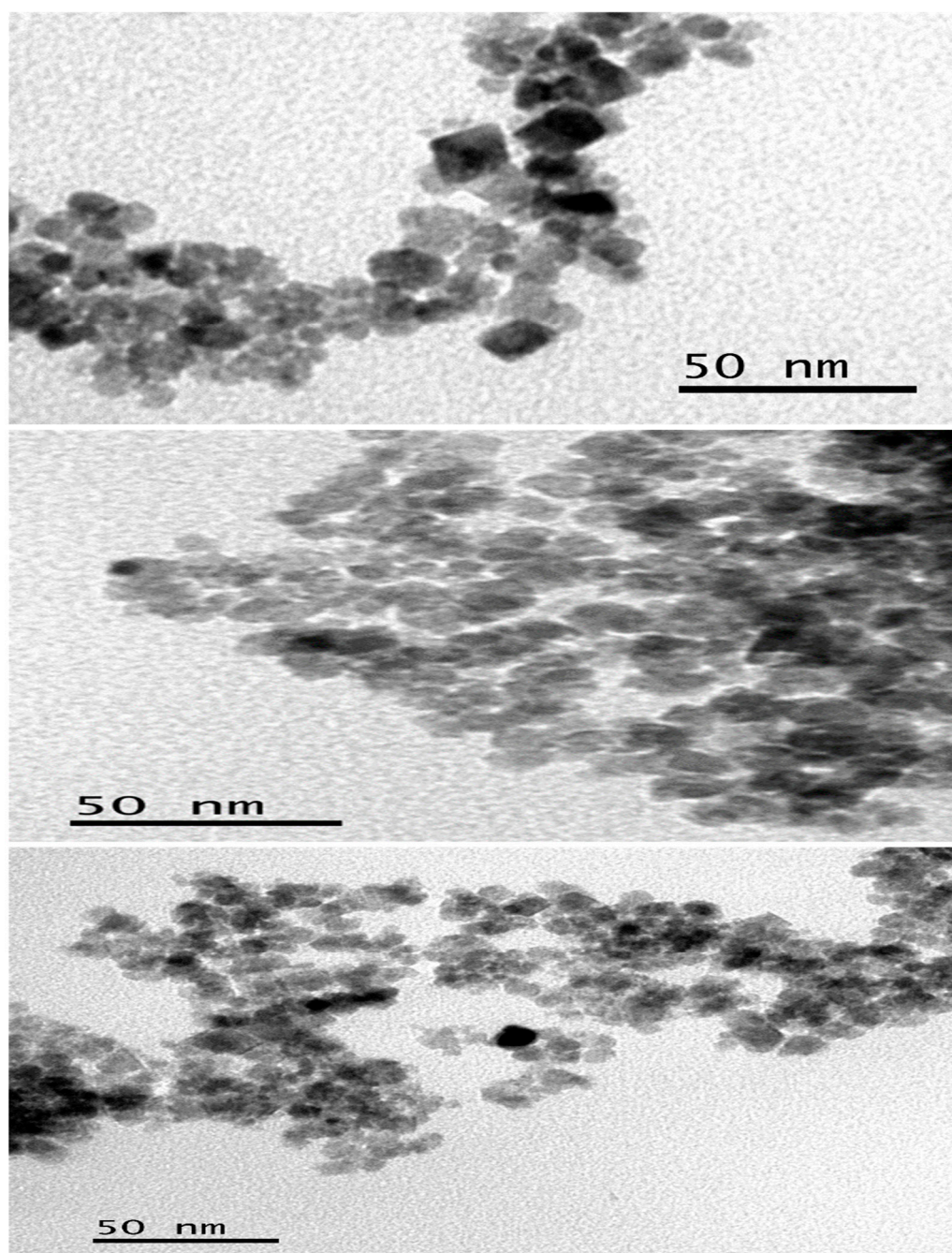
Figure 2. TEM images of OTA, DDT, and TOP-capped Fe_3O_4 nanoparticles.

FTIR was used to confirm the interaction of the capping agents with iron oxide nanoparticles (Figure S3). Two weak peaks observed at 3387 and 3283 cm^{-1} in the OTA-capped iron oxide nanoparticle spectrum are attributed to the asymmetric and symmetric modes of NH_2, respectively [36]. The asymmetric and symmetric C—H stretching vibrations of the alkyl chain of OTA are also observed at 2929 and 2833 cm^{-1}. However, in the Fe_3O_4-OTA nanoparticles spectrum, these peaks are shifted to 2937 and 2905 cm^{-1}. The C—N stretch of OTA appeared at 1477 cm^{-1}, which is shifted to 1469 cm^{-1} in the Fe_3O_4-OTA spectrum. This indicates the presence of octylamine on the surface of iron oxide nanoparticles [37]. DDT shows sharp bands at 2913 cm^{-1} and 2849 cm^{-1}, which are due to the asymmetric and symmetric C—H stretching modes, respectively [38,39]. These bands are blue-shifted by 16 and 8 cm^{-1}, respectively, in the Fe_3O_4-DDT nanoparticles spectrum. The C—S stretching vibration at 723 cm^{-1} observed in the DDT spectrum is

shifted to 826 cm^{-1} in the Fe$_3$O$_4$-DDT nanoparticles spectrum. The pure DDT also shows S—H stretching vibrational modes at 2564 cm^{-1} [40], which is shifted by 3 cm^{-1} in the Fe$_3$O$_4$-DDT nanoparticles spectrum. TOP exhibits C–P stretching vibrations at 1140 cm^{-1}, while the bands at 2913 cm^{-1} and 2857 cm^{-1} are attributed to C—H stretching vibrational modes [41]. The C—H stretching vibrations were observed at 2928 cm^{-1} and 2856 cm^{-1} in the Fe$_3$O$_4$-TOP nanoparticles spectrum, while the C—P absorption band was observed at 1139 cm^{-1}. The sharp bands at 552 cm^{-1} in iron oxide nanoparticles' spectra are attributed to Fe—O vibration [42].

3.2. Optical Properties

The optical absorption spectra of the as-prepared iron oxide nanoparticles in Figure 3a shows that Fe$_3$O$_4$–OTA, Fe$_3$O$_4$–DDT, and Fe$_3$O$_4$–TOP nanoparticles exhibit absorption peaks at 274, 210, and 209 nm, respectively. The peaks can be attributed to electrons moving from the oxygen atom to the *d*-metal orbital [43,44]. The optical band gaps estimated from Tauc plots (Figure 3b) were 2.25 eV for Fe$_3$O$_4$–OTA, 2.47 eV for Fe$_3$O$_4$–DDT, and 2.76 eV for Fe$_3$O$_4$–TOP. The band gap energy decreases with increasing capping agent chain length. The variation in absorption band edges and band gap energies may be due to the different morphologies of the nanoparticles. This indicates the modification of the valence band and conduction bands by the quantum confinement effect [45,46].
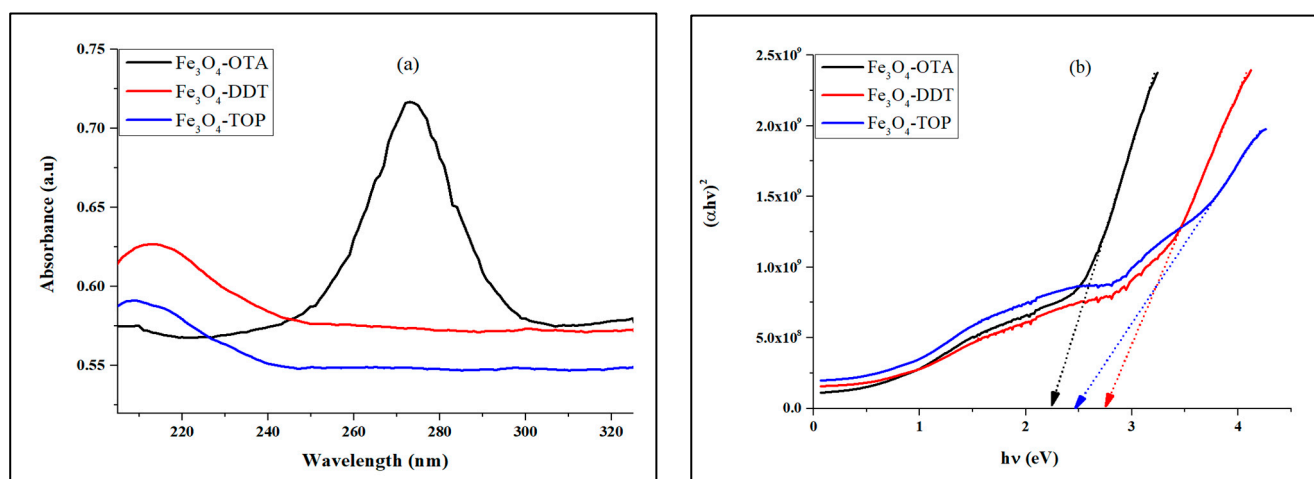
Figure 3. (**a**) UV-Vis spectra and (**b**) Tauc plots of iron OTA, DDT and TOP-capped iron oxide nanoparticles.

3.3. Adsorption Studies of Iron Oxide Nanoparticles

Adsorption is a surface phenomenon where pollutants transfer from a liquid phase to the surface of a solid phase via physical forces or chemical interactions [47]. Since photocatalytic degradation of contaminants takes place on the surface of the photocatalyst, the adsorption capacity test is crucial [48]. The Fe$_3$O$_4$ nano-photocatalysts reached equilibrium adsorption capacity for both methylene blue and methyl orange dyes at 45 min (Figure 4). The stability of Fe$_3$O$_4$ nanoparticles after 45 min demonstrates that the adsorption–desorption equilibrium has been attained.

3.4. Photocatalytic Degradation of Methylene Blue and Methyl Orange by Iron Oxide Nanoparticles

The photocatalytic activity of OTA, DDT and TOP-capped iron oxide nanoparticles was evaluated using methylene blue (MB) and methyl orange (MO) dyes as organic pollutants under visible light irradiation. The time-dependent absorption spectra of MB and MO show (Figures S4 and S5) a decrease in characteristic absorption peaks over time. In the absence of iron oxide nanoparticles, the degradation of the dyes was insignificant. However, the dyes degraded significantly in the presence of iron oxide nanoparticles, as indicated by

the C_t/C_0 plot (Figure S6). The degradation efficiencies of MB by the iron oxide nanoparticles after 180 min irradiation are 55.5%, 58.3% and 66.7% by Fe_3O_4-OTA, Fe_3O_4-DDT, and Fe_3O_4-TOP, respectively (Figure 5a). The degradation efficiency is observed to increase with an increase in the chain length of the capping agent. The highest degradation efficiency of methylene blue obtained in this study is slightly higher than that of previous studies using γ–Fe_2O_3 nanoparticles (38%) [49], hematite iron oxide nanoparticles (51%) [50], and Fe_3O_4/ZnO nanocomposite (63%) [51]. Degradation efficiencies of 63.8%, 47.7%, and 74.1% were obtained for Fe_3O_4-OTA, Fe_3O_4-DDT, and Fe_3O_4-TOP, respectively, against MO dye (Figure 5b). OTA and TOP-capped iron oxide nanoparticles exhibit superior activity against MO compared to Fe_3O_4-DDT, and this could be due to Fe_3O_4-DDT's large band gap. The nanoparticles' agglomeration impacts their optical properties, which affects their capacity to absorb and disperse the incident radiation as well as their photocatalytic performance [52–54]. Therefore, the high photocatalytic degradation efficiency demonstrated by Fe_3O_4-TOP for both MB and MO dyes could be due to the Fe_3O_4-TOP nanoparticle morphology and light absorption capacity.
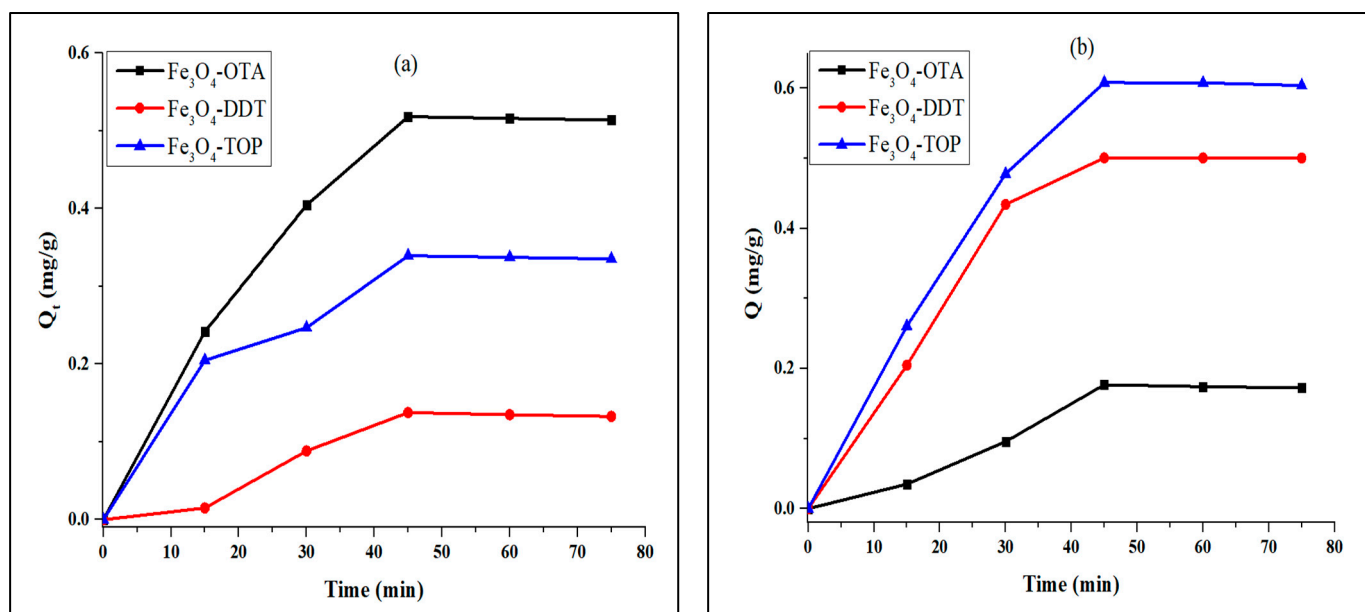

Figure 4. Time profile of (**a**) methylene blue and (**b**) methyl orange adsorption.

The photocatalytic degradation reaction of MB and MO follows a pseudo-first-order kinetic model as demonstrated by the linear correlation of the graphs of $\ln(C_t/C_0)$ over irradiation time. Equation (3) was used to calculate the rate constants.

$$\ln\left(\frac{C_t}{C_0}\right) = -kt \tag{3}$$

The rate constants and correlation coefficients (R^2) determined from the graphs in Figure S7 are shown in Table 1. The photodegradation rate constants of cationic dye are 4.28×10^{-3} min^{-1} for Fe_3O_4-OTA, 5.01×10^{-3} min^{-1} for Fe_3O_4-DDT, and 5.57×10^{-3} min^{-1} for Fe_3O_4-TOP, while the photodegradation rate constants of anionic dye are 0.00529 min^{-1} for Fe_3O_4-OTA, 3.96×10^{-3} min^{-1} for Fe_3O_4-DDT, and 7.76×10^{-3} min^{-1} for Fe_3O_4-TOP. The degradation rate constant of Fe_3O_4-DDT is low in the anionic dye but higher in the cationic dye, which is consistent with the degradation efficiency plot. The high correlation coefficient values show that the photodegradation of MB and MO dyes fits the pseudo-first-order kinetic model.
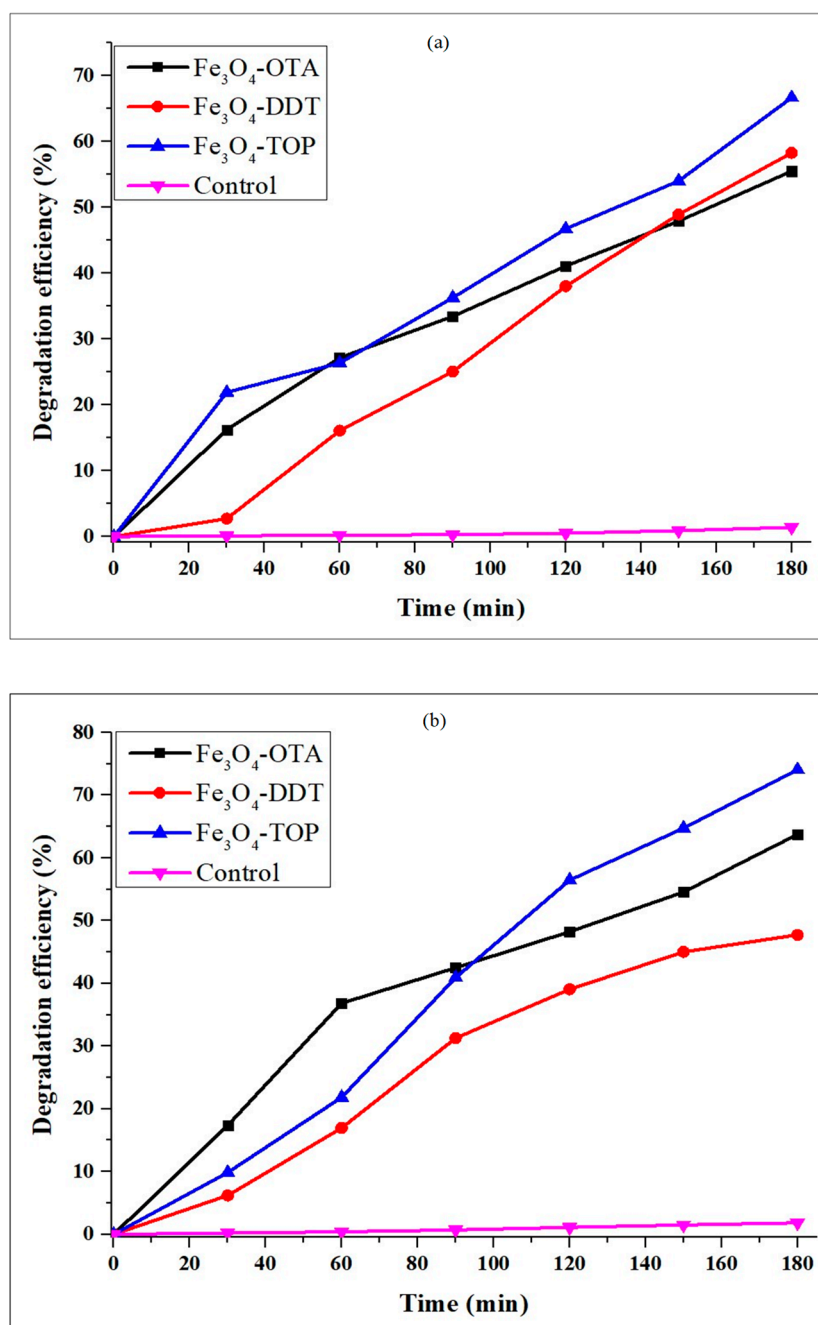
Figure 5. Degradation efficiency curves of (**a**) MB and (**b**) MO.

Table 1. Photodegradation rate constants and correlation coefficients of MB and MO by iron oxide nanoparticles.

Dye	Catalyst	Degradation Efficiency (%)	Rate Constant (min^{-1})	R^2
Methylene blue	Fe_3O_4-OTA	55.5	4.28×10^{-3}	99.69×10^{-2}
	Fe_3O_4-DDT	58.3	5.01×10^{-3}	98.41×10^{-2}
	Fe_3O_4-TOP	66.7	5.57×10^{-3}	98.50×10^{-2}
Methyl orange	Fe_3O_4-OTA	63.8	5.29×10^{-3}	98.89×10^{-2}
	Fe_3O_4-DDT	47.7	3.96×10^{-3}	98.97×10^{-2}
	Fe_3O_4-TOP	74.1	7.76×10^{-3}	98.95×10^{-2}

3.5. Effect of Scavengers on the Photocatalytic Degradation of Dyes

A series of scavengers were added to the dye solutions to determine the active species in the photocatalytic degradation of methylene blue and methyl orange dyes by the as-prepared iron oxide nanoparticles. The results were contrasted to dye degradation efficiency obtained using only iron oxide nanoparticles, as shown in Figure 6. Silver nitrate (SN), iso-propanol alcohol (IPA), ascorbic acid (AA), and ethylenediaminetetraacetic acid disodium salt (EDTA-2Na) were used to detect e^-, $\bullet OH$, $\bullet O_2^-$, and h^+ scavenging activity [55]. MB dye degradation efficiency by the as-prepared iron oxide nanoparticles decreases from 66.7–55.5% to 10.8–7.2% (SN), 22.9–19.7% (AA), 58.4–43.4% (EDTA), and 13.9–8.1% (IPA). The addition of scavengers also decreased the reaction rate constants as presented in Table 2 (Figure S8). This demonstrates that e^- and $\bullet OH$ are the main active species for the degradation of MB for all the as-prepared Fe_3O_4 nanoparticles. The results are consistent with previous studies using other photocatalysts [56,57]. However, the degradation efficiency of MO by Fe_3O_4–OTA decreases from 63.8% to 18.5% (SN), 43.7% (AA), 16.7% (EDTA), and 12.9% (IPA), whereas with Fe_3O_4–DDT the degradation efficiency decreases from 47.7% to 15.3% (SN), 34.7% (AA), 22.4% (EDTA), and 17.5% (IPA). The photocatalytic degradation efficiency of MO by Fe_3O_4–TOP decreases from 74.1% to 6.4% (SN), 42.7% (AA), 21.5% (EDTA), and 11.3% (IPA). In the presence of an ascorbic acid (AA) scavenger, Fe_3O_4-TOP exhibited a reaction rate of 1.58×10^{-2} min^{-1} (Figure S9), which is higher than the dye degradation rate without the scavenger; however, the degradation efficiency percentage remained low. The results indicate that e^- and $\bullet OH$ play significant roles in the degradation of MO using Fe_3O_4–DDT and Fe_3O_4–TOP, while $\bullet OH$ and h^+ are observed to be the main active species with e^- acting as the secondary active species for Fe_3O_4–OTA.
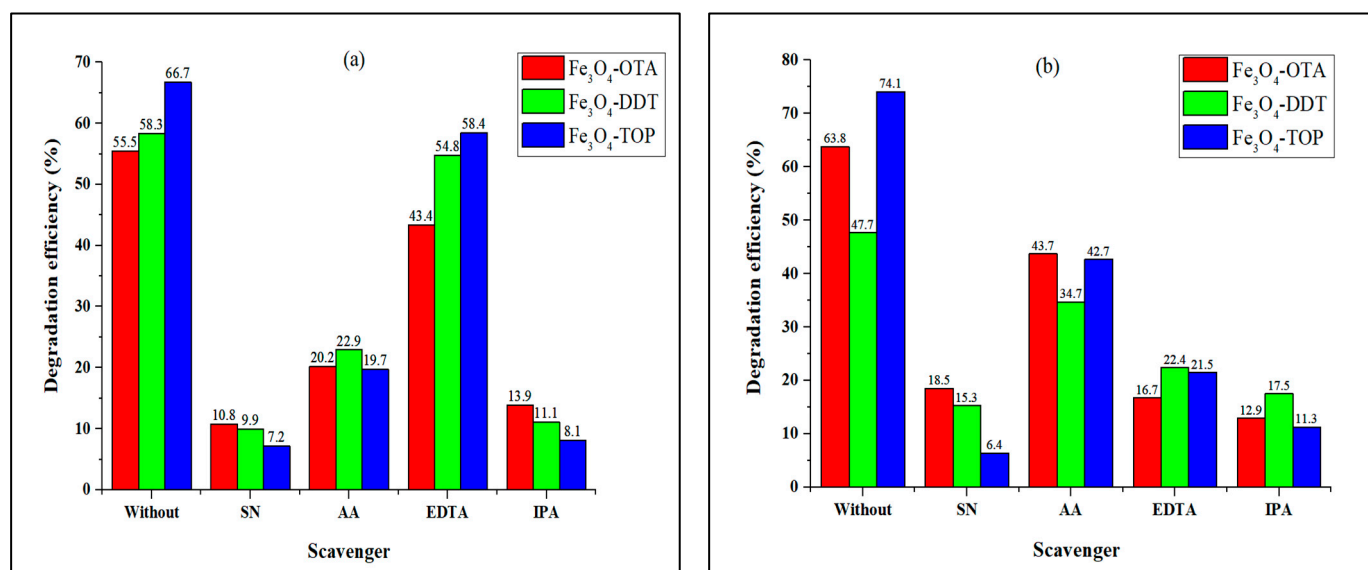
Figure 6. Effects of scavengers on the photodegradation of (**a**) MB and (**b**) MO by iron oxide nanoparticles.
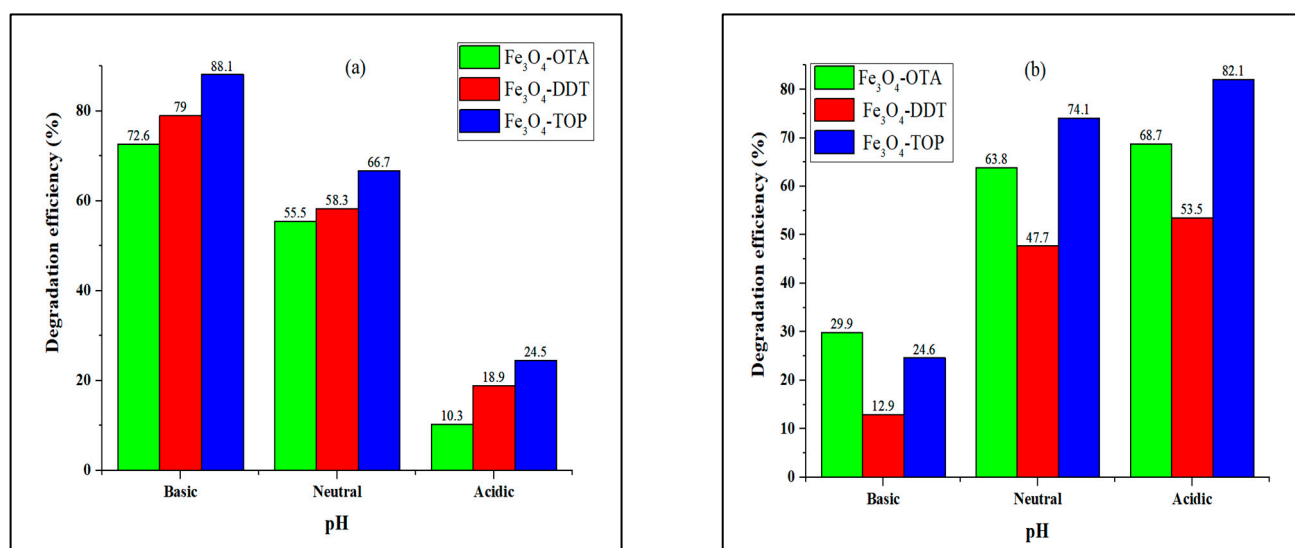
3.6. Effect of pH

Another variable that influences the efficiency of the catalyst charge surface, dye adsorption, and other photocatalytic reaction parameters is pH [58]. Figure 7 shows the results of a study on the photocatalytic degradation of MB and MO at various pH levels between 2 and 10 in the presence of iron oxide nanoparticles. For MB dye, low degradation efficiencies of 10.3–24.5% were obtained at pH 2 and high degradation efficiencies of 72.6% for Fe_3O_4-OTA, 79.0% for Fe_3O_4-DDT, and 88.1% for Fe_3O_4-TOP were obtained at pH 10. The higher degradation efficiency of MB degradation at pH 10 can be attributed to the enhanced adsorption of MB dye molecules on the negatively charged catalyst surface, resulting in a strong interaction between the photocatalyst and the generated radicals,

resulting in rapid degradation [35]. In contrast, at pH 2, the existence of additional h^+ in the reaction mixture made the catalyst surface more positive, inhibiting dye molecule adsorption due to columbic repulsion interactions, which resulted in a slower rate of radical generation and therefore degradation [59]. In contrast, the degradation efficiency of MO was observed to increase with decreasing pH, and the highest efficiency of 82.1% for Fe_3O_4-TOP was obtained at pH 2. The pH value has a major influence on the existing forms of methyl orange; in an acidic medium, it is in quinoid form, and it progressively transitioned to an azo structure as the pH of the solution increased [60,61]. In comparison to methyl orange in azo form, the quinoid structure is easier to degrade [62]. Hence, in an acidic medium, methyl orange dye degradation efficiency was higher.

Table 2. Photodegradation rate constants of MB and MO by iron oxide nanoparticles in the presence of scavengers.

Dye	Catalyst	Rate Constant (min^{-1})			
		SN	AA	EDTA	IPA
Methylene blue	Fe_3O_4-OTA	6.15×10^{-4}	1.84×10^{-3}	3.18×10^{-3}	8.54×10^{-4}
	Fe_3O_4-DDT	1.12×10^{-3}	1.36×10^{-3}	4.68×10^{-3}	6.84×10^{-4}
	Fe_3O_4-TOP	4.39×10^{-4}	$9.08 \times 10{-4}$	4.78×10^{-3}	5.62×10^{-4}
Methyl orange	Fe_3O_4-OTA	1.26×10^{-3}	3.38×10^{-3}	9.97×10^{-4}	7.66×10^{-4}
	Fe_3O_4-DDT	9.53×10^{-4}	2.51×10^{-3}	1.42×10^{-3}	1.18×10^{-3}
	Fe_3O_4-TOP	3.52×10^{-4}	1.58×10^{-2}	1.47×10^{-3}	6.61×10^{-4}

Figure 7. Effect of pH on (**a**) MB and (**b**) MO photocatalytic degradation by iron oxide nanoparticles.

3.7. Photostability Studies

Photostability is a critical property of photocatalysts which makes photocatalysis a cost-effective, practical, and sustainable water treatment method [63]. Hence, recyclability studies were conducted to evaluate the iron oxide nanoparticles' stability. Figure 8 demonstrates that the photodegradation efficiencies of the MB and MO dyes remained steady until the third cycle, with only a 0.8–11.3% decrease in efficiency over the three cycles. The decrease in photocatalytic degradation efficiency over the three cycles could be ascribed to either the build-up of intermediate products on the particle surface or nanoparticle loss during washing and filtration [64].
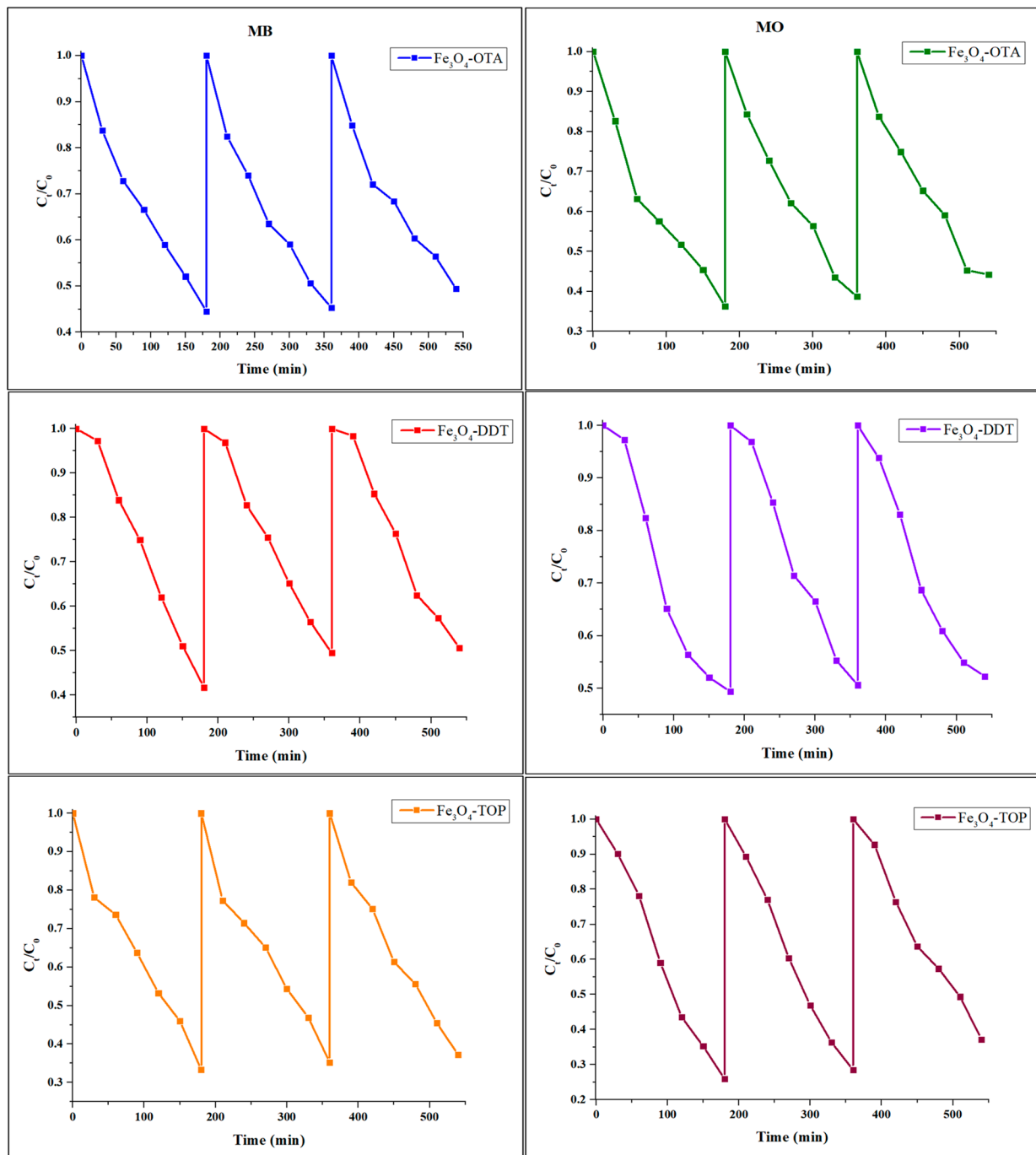
Figure 8. The recyclability of iron oxide nano-photocatalysts.

4. Conclusions

Iron oxide nanoparticles were prepared by co-precipitation method using three different capping agents to study the effect of capping agents on the morphological, optical, and photocatalytic properties of the as-prepared iron oxide nanoparticles. Powder X-ray diffraction patterns of the as-prepared iron oxide nanoparticles confirmed the cubic inverse spinel structure of Fe_3O_4. TEM images revealed Fe_3O_4-OTA nanoparticles are a mixture of square-like, oval, and quasi-spherical particles with an average particle size of 2.1 nm. Fe_3O_4-DDT nanoparticles were agglomerated quasi-spherical shapes with a mean size of 5.0 nm. The Fe_3O_4-TOP nanoparticles were also agglomerated and irregularly shaped with particle sizes of 4.4 nm. The results show that the use of different capping agents

results in different particle sizes and shapes of the iron oxide nanoparticles. FTIR spectra confirmed the octylamine, 1-dodecanethiol, and tri-*n*-octylphosphine bond to the surface of the as-prepared iron oxide nanoparticles. Bandgap energies of 2.25, 2.47, and 2.76 eV were obtained for Fe_3O_4-OTA, Fe_3O_4-DDT, and Fe_3O_4-TOP, respectively. The results reveal that the bandgap energy can be tuned using different capping agents due to variations in the morphology of the nanoparticles obtained. The as-prepared iron oxide nanoparticles were used as photocatalysts for the degradation of MB and MO. The results showed that Fe_3O_4-TOP exhibited high degradation efficiency for the degradation of MB (66.7%) and MO (74.1%). The role of scavengers on the photocatalytic degradation efficiency was also investigated and e^- and $\bullet OH$ were found to be the major active species in the photodegradation reaction of MB for all Fe_3O_4 nanoparticles, respectively, whereas, for MO, $\bullet OH$ and h^+ were found to be the major active species when using Fe_3O_4-OTA. The as-prepared Fe_3O_4 nano-photocatalysts are photostable and recyclable for the photocatalytic degradation of the organic dyes.

Supplementary Materials: The following supporting information can be downloaded at: https://www.mdpi.com/article/10.3390/nano13142067/s1, Figure S1. Size distribution histograms of OTA, DDT and TOP-capped iron oxide nanoparticles. Figure S2. TEM image of uncapped iron oxide nanoparticles. Figure S3. FTIR spectra overlay of octylamine, 1-dodecanethiol and tri-n-octylphosphine capped iron oxide nanoparticles. Figure S4. Absorption spectra of methylene blue (MB) over (a) Fe_3O_4-OTA, (b) Fe_3O_4-DDT and (c) Fe_3O_4-TOP nanoparticles. Figure S5. Absorption spectra of methyl orange (MO) over (a) Fe_3O_4-OTA, (b) Fe_3O_4-DDT and (c) Fe_3O_4-TOP nanoparticles. Figure S6. (a) MB and (b) MO C_t/C_0) versus irradiation time plots. Figure S7. Methylene blue (a) and methyl orange (b) photocatalytic degradation kinetics using iron oxide nanoparticles as photocatalysts. Figure S8. Photodegradation kinetics plots of MB by iron oxide nanoparticles in the presence of scavengers. Figure S9. Photodegradation kinetics plots of MO by iron oxide nanoparticles in the presence of scavengers.

Author Contributions: P.A.A.; conceptualization, supervision, writing—review and editing, funding acquisition. T.B.M.; data curation, formal analysis, writing—draft preparation. All authors have read and agreed to the published version of the manuscript.

Data Availability Statement: All research data are presented in the paper and the supplementary data.

Conflicts of Interest: The authors declare no conflict of interest.

References

1. Bruno, A.; Agostinetto, G.; Fumagalli, S.; Ghisleni, G.; Sandionigi, A. It's a long way to the tap: Microbiome and DNA-based omics at the core of drinking water quality. *Int. J. Environ. Res. Public Health* **2022**, *19*, 7940. [CrossRef] [PubMed]
2. Dagher, L.A.; Hassan, J.; Kharroubi, S.; Jaafar, H.; Kassem, I.I. Nationwide assessment of water quality in rivers across Lebanon by quantifying fecal indicators densities and profiling antibiotic resistance of *Escherichia coli*. *Antibiotics* **2021**, *10*, 883. [CrossRef] [PubMed]
3. Islam, T.; Repon, M.R.; Islam, T.; Sarwar, Z.; Rahman, M.M. Impact of textile dyes on health and ecosystem: A review of structure, causes, and potential solutions. *Environ. Sci. Pollut. Res.* **2023**, *30*, 9207–9242. [CrossRef]
4. Al-Tohamy, R.; Ali, S.S.; Li, F.; Okasha, K.M.; Mahmoud, Y.A.G.; Elsamahy, T.; Jiao, H.; Fu, Y.; Sun, J. A critical review on the treatment of dye-containing wastewater: Ecotoxicological and health concerns of textile dyes and possible remediation approaches for environmental safety. *Ecotoxicol. Environ. Saf.* **2022**, *231*, 113160. [CrossRef]
5. Elgarahy, A.M.; Elwakeel, K.Z.; Mohammad, S.H.; Elshoubaky, G.A. A critical review of biosorption of dyes, heavy metals and metalloids from wastewater as an efficient and green process. *Clean. Eng. Technol.* **2021**, *4*, 100209. [CrossRef]
6. Khan, M.D.; Singh, A.; Khan, M.Z.; Tabraiz, S.; Sheikh, J. Current perspectives, recent advancements, and efficiencies of various dye-containing wastewater treatment technologies. *J. Water Process. Eng.* **2023**, *53*, 103579. [CrossRef]
7. Khan, S.; Naushad, M.; Govarthanan, M.; Iqbal, J.; Alfadul, S.M. Emerging contaminants of high concern for the environment: Current trends and future research. *Environ. Res.* **2022**, *207*, 112609. [CrossRef]
8. Markandeya; Mohan, D.; Shukla, S.P. Hazardous consequences of textile mill effluents on soil and their remediation approaches. *Clean. Eng. Technol.* **2022**, *7*, 100434. [CrossRef]

9. Oladoye, P.O.; Ajiboye, T.O.; Omotola, E.O.; Oyewola, O.J. Methylene blue dye: Toxicity and potential elimination technology from wastewater. *Results Eng.* **2022**, *16*, 100678. [CrossRef]

10. Sharma, M.; Poddar, M.; Gupta, Y.; Nigam, S.; Avasthi, D.K.; Adelung, R.; Abolhassani, R.; Fiutowski, J.; Joshi, M.; Mishra, Y.K. Solar light assisted degradation of dyes and adsorption of heavy metal ions from water by CuO–ZnO tetrapodal hybrid nanocomposite. *Mater. Today Chem.* **2020**, *17*, 100336. [CrossRef]

11. Smazna, D.; Shree, S.; Polonskyi, O.; Lamaka, S.; Baum, M.; Zheludkevich, M.; Faupel, F.; Adelung, R.; Mishra, Y.K. Mutual interplay of ZnO micro- and nanowires and methylene blue during cyclic photocatalysis process. *J. Environ. Chem. Eng.* **2019**, *7*, 103016. [CrossRef]

12. Li, Z.; Liu, D.; Huang, W.; Wei, X.; Huang, W. Biochar supported CuO composites used as an efficient peroxymonosulfate activator for highly saline organic wastewater treatment. *Sci. Total Environ.* **2020**, *721*, 137764. [CrossRef] [PubMed]

13. Kiani, R.; Mirzaei, F.; Ghanbari, F.; Feizi, R.; Mehdipour, F. Real textile wastewater treatment by a sulfate radicals-Advanced Oxidation Process: Peroxydisulfate decomposition using copper oxide (CuO) supported onto activated carbon. *J. Water Process Eng.* **2020**, *38*, 101623. [CrossRef]

14. Chandra, R.; Singh, V.; Tomar, S.; Nath, M. Multi-core-shell composite SnO₂NPs@ZIF-8: Potential antiviral agent and effective photocatalyst for waste-water treatment. *Environ. Sci. Pollut. Res.* **2019**, *26*, 23346–23358. [CrossRef]

15. Mousa, H.M.; Alenezi, J.F.; Mohamed, I.M.A.; Yasin, A.S.; Hashem, A.-F.M.; Abdal-hay, A. Synthesis of TiO₂@ZnO heterojunction for dye photodegradation and wastewater treatment. *J. Alloys Compd.* **2021**, *886*, 161169. [CrossRef]

16. Balakrishnan, A.; Appunni, S.; Chinthala, M.; Vo, D.-V.N. Biopolymer-supported TiO₂ as a sustainable photocatalyst for wastewater treatment: A review. *Environ. Chem. Lett.* **2022**, *20*, 3071–3098. [CrossRef]

17. Noreen, S.; Khalid, U.; Ibrahim, S.M.; Javed, T.; Ghani, A.; Naz, S.; Iqbal, M. ZnO, MgO and FeO adsorption efficiencies for direct sky Blue dye: Equilibrium, kinetics and thermodynamics studies. *J. Mater. Res. Technol.* **2020**, *9*, 5881–5893. [CrossRef]

18. Mohadesi, M.; Gouran, A.; Seifi, K. Removal of ibuprofen from synthetic wastewater using photocatalytic method in the presence of FeO photocatalyst supported on modified Iranian clinoptilolite. *Environ. Sci. Pollut. Res.* **2022**, *29*, 34338–34348. [CrossRef]

19. Naseem, T.; Durrani, T. The role of some important metal oxide nanoparticles for wastewater and antibacterial applications: A review. *J. Environ. Chem. Ecotoxicol.* **2021**, *3*, 59–75. [CrossRef]

20. Leonel, A.G.; Mansur, A.A.P.; Mansur, H.S. Advanced functional nanostructures based on magnetic iron oxide nanomaterials for water remediation: A review. *Water Res.* **2021**, *190*, 116693. [CrossRef]

21. Qumar, U.; Hassan, J.Z.; Bhatti, R.A.; Raza, A.; Nazir, G.; Nabgan, W.; Ikram, M. Photocatalysis vs adsorption by metal oxide nanoparticles. *Mater. Sci. Technol.* **2022**, *131*, 122–166. [CrossRef]

22. Jabbar, Z.H.; Esmail Ebrahim, S. Recent advances in nano-semiconductors photocatalysis for degrading organic contaminants and microbial disinfection in wastewater: A comprehensive review. *Environ. Nanotechnol. Monit. Manag.* **2022**, *17*, 100666. [CrossRef]

23. You, J.; Wang, L.; Zhao, Y.; Bao, W. A review of amino-functionalized magnetic nanoparticles for water treatment: Features and prospects. *J. Clean. Prod.* **2021**, *281*, 124668. [CrossRef]

24. Sodipo, B.K.; Noqta, O.A.; Aziz, A.A.; Katsikini, M.; Pinakidou, F.; Paloura, E.C. Influence of capping agents on fraction of Fe atoms occupying octahedral site and magnetic property of magnetite (Fe₃O₄) nanoparticles by one-pot co-precipitation method. *J. Alloys Compd.* **2023**, *938*, 168558. [CrossRef]

25. Sharma, P.; Kumari, S.; Ghosh, D.; Yadav, V.; Vij, A.; Rawat, P.; Kumar, S.; Sinha, C.; Saini, S.; Sharma, V.; et al. Capping agent-induced variation of physicochemical and biological properties of α-Fe₂O₃ nanoparticles. *Mater. Chem. Phys.* **2021**, *258*, 123899. [CrossRef]

26. Guidolin, T.O.; Possolli, N.M.; Polla, M.B.; Wermuth, T.B.; Franco de Oliveira, T.; Eller, S.; Klegues Montedo, O.R.; Arcaro, S.; Cechinel, M.A.P. Photocatalytic pathway on the degradation of methylene blue from aqueous solutions using magnetite nanoparticles. *J. Clean. Prod.* **2021**, *318*, 128556. [CrossRef]

27. Rivera, F.L.; Recio, F.J.; Palomares, F.J.; Sánchez-Marcos, J.; Menéndez, N.; Mazarío, E.; Herrasti, P. Fenton-like degradation enhancement of methylene blue dye with magnetic heating induction. *J. Electroanal. Chem.* **2020**, *879*, 114773. [CrossRef]

28. Modrogan, C.; Căprărescu, S.; Dăncilă, A.M.; Orbuleț, O.D.; Grumezescu, A.M.; Purcar, V.; Radițoiu, V.; Fierascu, R.C. Modified Composite Based on Magnetite and Polyvinyl Alcohol: Synthesis, Characterization, and Degradation Studies of the Methyl Orange Dye from Synthetic Wastewater. *Polymers* **2021**, *13*, 3911. [CrossRef]

29. León-Flores, J.; Pérez-Mazariego, J.L.; Marquina, M.; Gómez, R.; Escamilla, R.; Tehuacanero-Cuapa, S.; Reyes-Damián, C.; Arenas-Alatorre, J. Controlled Formation of Hematite—Magnetite Nanoparticles by a Biosynthesis Method and Its Photocatalytic Removal Potential Against Methyl Orange Dye. *J. Cluster Sci.* **2022**, 1–15. [CrossRef]

30. Kusior, A.; Michalec, K.; Jelen, P.; Radecka, M. Shaped Fe₂O₃ nanoparticles—Synthesis and enhanced photocatalytic degradation towards RhB. *Appl. Surf. Sci.* **2019**, *476*, 342–352. [CrossRef]

31. Arévalo, P.; Isasi, J.; Caballero, A.C.; Marco, J.F.; Martín-Hernández, F. Magnetic and structural studies of Fe₃O₄ nanoparticles synthesized via coprecipitation and dispersed in different surfactants. *Ceram. Int.* **2017**, *43*, 10333–10340. [CrossRef]

32. Stanley, R.; Jebasingh, J.A.; Vidyavathy, S.M. Cost-effective and sunlight-driven degradation of anionic and cationic dyes with pure ZnO nanoparticles. *Int. J. Environ. Sci. Technol.* **2022**, *19*, 11249–11262. [CrossRef]

33. Elizondo-Villarreal, N.; Verástegui-Domínguez, L.; Rodríguez-Batista, R.; Gándara-Martínez, E.; Alcorta-García, A.; Martínez-Delgado, D.; Rodríguez-Castellanos, E.A.; Vázquez-Rodríguez, F.; Gómez-Rodríguez, C. Green Synthesis of Magnetic Nanoparti-

cles of Iron Oxide Using Aqueous Extracts of Lemon Peel Waste and Its Application in Anti-Corrosive Coatings. *Materials* **2022**, *15*, 8328. [CrossRef] [PubMed]

34. Besenhard, M.O.; Panariello, L.; Kiefer, C.; LaGrow, A.P.; Storozhuk, L.; Perton, F.; Begin, S.; Mertz, D.; Thanh, N.T.K.; Gavriilidis, A. Small iron oxide nanoparticles as MRI T1 contrast agent: Scalable inexpensive water-based synthesis using a flow reactor. *Nanoscale* **2021**, *13*, 8795–8805. [CrossRef]

35. Kumar, A.P.; Ahmed, F.; Kumar, S.; Anuradha, G.; Harish, K.; Kumar, B.P.; Lee, Y.-I. Synthesis of magnetically recoverable Ru/Fe_3O_4 nanocomposite for efficient photocatalytic degradation of methylene blue. *J. Cluster Sci.* **2022**, *33*, 853–865. [CrossRef]

36. Dhiman, A.; Sharma, A.K.; Bhardwaj, D.; Agrawal, G. Biodegradable dual stimuli responsive alginate based microgels for controlled agrochemicals release and soil remediation. *Int. J. Biol. Macromol.* **2023**, *228*, 323–332. [CrossRef]

37. Chen, D.; Ren, X.; Li, T.; Chen, Z.; Cao, Y.; Xu, F. Octylamine-Supporting Interlayer Expanded Molybdenum Diselenide as a High-Power Cathode for Rechargeable Mg Batteries. *Energy Environ. Mater.* **2022**, e12486. [CrossRef]

38. Chen, L.; Li, G. Functions of 1-Dodecanethiol in the Synthesis and Post-Treatment of Copper Sulfide Nanoparticles Relevant to Their Photocatalytic Applications. *ACS Appl. Nano Mater.* **2018**, *1*, 4587–4593. [CrossRef]

39. Hu, S.; Chen, Z.; Guo, X. Inhibition Effect of Three-Dimensional (3D) Nanostructures on the Corrosion Resistance of 1-Dodecanethiol Self-Assembled Monolayer on Copper in NaCl Solution. *Materials* **2018**, *11*, 1225. [CrossRef]

40. Luo, D.; Luo, Y.; Lu, X.; Shi, M.; Wei, J.; Lu, Z.; Huang, Y.; Ni, Y. Cooperative selective benzyl alcohol oxidation and hydrogen production over $Pd_6(SC_{12}H_{25})_{12}$ cluster-coupled CdS nanorods: The key role of water in photocatalytic benzyl alcohol splitting. *J. Mater. Chem.* **2022**, *10*, 15941–15948. [CrossRef]

41. Ji, Y.; Wang, M.; Yang, Z.; Qiu, H.; Padhiar, M.A.; Zhou, Y.; Wang, H.; Dang, J.; Gaponenko, N.V.; Bhatti, A.S. Trioctylphosphine-Assisted Pre-protection Low-Temperature Solvothermal Synthesis of Highly Stable $CsPbBr_3/TiO_2$ Nanocomposites. *J. Phys. Chem. Lett.* **2021**, *12*, 3786–3794. [CrossRef]

42. Ananthi, S.; Kavitha, M.; Kumar, E.R.; Balamurugan, A.; Al-Douri, Y.; Alzahrani, H.K.; Keshk, A.A.; Habeebullah, T.M.; Abdel-Hafez, S.H.; El-Metwaly, N.M. Natural tannic acid (green tea) mediated synthesis of ethanol sensor based Fe_3O_4 nanoparticles: Investigation of structural, morphological, optical properties and colloidal stability for gas sensor application. *Sens. Actuators B Chem.* **2022**, *352*, 131071. [CrossRef]

43. Mizuno, S.; Yao, H. On the electronic transitions of α-Fe_2O_3 hematite nanoparticles with different size and morphology: Analysis by simultaneous deconvolution of UV–vis absorption and MCD spectra. *J. Magn. Magn.* **2021**, *517*, 167389. [CrossRef]

44. Kashyap, S.J.; Sankannavar, R.; Madhu, G.M. Iron oxide (Fe_2O_3) synthesized via solution-combustion technique with varying fuel-to-oxidizer ratio: FT-IR, XRD, optical and dielectric characterization. *Mater. Chem. Phys.* **2022**, *286*, 126118. [CrossRef]

45. Andrade Neto, N.F.; Nascimento, L.E.; Correa, M.; Bohn, F.; Bomio, M.R.D.; Motta, F.V. Characterization and photocatalytic application of Ce^{4+}, Co^{2+}, Mn^{2+} and Ni^{2+} doped Fe_3O_4 magnetic nanoparticles obtained by the co-precipitation method. *Mater. Chem. Phys.* **2020**, *242*, 122489. [CrossRef]

46. Suman; Chahal, S.; Kumar, A.; Kumar, P. Zn Doped α-Fe_2O_3: An Efficient Material for UV Driven Photocatalysis and Electrical Conductivity. *Crystals* **2020**, *10*, 273. [CrossRef]

47. Adeola, A.O.; Abiodun, B.A.; Adenuga, D.O.; Nomngongo, P.N. Adsorptive and photocatalytic remediation of hazardous organic chemical pollutants in aqueous medium: A review. *J. Contam. Hydrol.* **2022**, *248*, 104019. [CrossRef]

48. Pavel, M.; Anastasescu, C.; State, R.-N.; Vasile, A.; Papa, F.; Balint, I. Photocatalytic Degradation of Organic and Inorganic Pollutants to Harmless End Products: Assessment of Practical Application Potential for Water and Air Cleaning. *Catalysts* **2023**, *13*, 380. [CrossRef]

49. Rehman, A.; Daud, A.; Warsi, M.F.; Shakir, I.; Agboola, P.O.; Sarwar, M.I.; Zulfiqar, S. Nanostructured maghemite and magnetite and their nanocomposites with graphene oxide for photocatalytic degradation of methylene blue. *Mater. Chem. Phys.* **2020**, *256*, 123752. [CrossRef]

50. Shenoy, M.; Sakunthala, A.; Vidhya, B.; Rajesh, S.; Raju, N.; Parthasarathi, S.K.; Sasikumar, M.; Govindan, K.; Tamilarasan, S.; Selvaraju, T.; et al. Visible light sensitive hexagonal boron nitride (hBN) decorated Fe_2O_3 photocatalyst for the degradation of methylene blue. *J. Mater. Sci. Mater. Electron.* **2021**, *32*, 1–18. [CrossRef]

51. Długosz, O.; Szostak, K.; Krupiński, M.; Banach, M. Synthesis of Fe_3O_4/ZnO nanoparticles and their application for the photodegradation of anionic and cationic dyes. *Int. J. Environ. Sci. Technol.* **2021**, *18*, 561–574. [CrossRef]

52. Pellegrino, F.; Pellutiè, L.; Sordello, F.; Minero, C.; Ortel, E.; Hodoroaba, V.-D.; Maurino, V. Influence of agglomeration and aggregation on the photocatalytic activity of TiO_2 nanoparticles. *Appl. Catal. B* **2017**, *216*, 80–87. [CrossRef]

53. Acosta-Herazo, R.; Mueses, M.Á.; Puma, G.L.; Machuca-Martínez, F. Impact of photocatalyst optical properties on the efficiency of solar photocatalytic reactors rationalized by the concepts of initial rate of photon absorption (IRPA) dimensionless boundary layer of photon absorption and apparent optical thickness. *Chem. Eng. J.* **2019**, *356*, 839–849. [CrossRef]

54. Ceballos-Chuc, M.C.; Ramos-Castillo, C.M.; Rodríguez-Pérez, M.; Ruiz-Gómez, M.Á.; Rodríguez-Gattorno, G.; Villanueva-Cab, J. Synergistic Correlation in the Colloidal Properties of TiO_2 Nanoparticles and Its Impact on the Photocatalytic Activity. *Inorganics* **2022**, *10*, 125. [CrossRef]

55. Jebasingh, R.S.; Stanley, P.K.; Ponmani, P.; Shekinah, M.E.; Vasanthi, J. Excellent Photocatalytic degradation of Methylene Blue, Rhodamine B and Methyl Orange dyes by Ag-ZnO nanocomposite under natural sunlight irradiation. *Optik* **2021**, *231*, 166518. [CrossRef]

56. Ma, Z.; Hu, L.; Li, X.; Deng, L.; Fan, G.; He, Y. A novel nano-sized MoS_2 decorated Bi_2O_3 heterojunction with enhanced photocatalytic performance for methylene blue and tetracycline degradation. *Ceram. Int.* **2019**, *45*, 15824–15833. [CrossRef]

57. Alshehri, A.A.; Malik, M.A. Biogenic fabrication of ZnO nanoparticles using Trigonella foenum-graecum (Fenugreek) for proficient photocatalytic degradation of methylene blue under UV irradiation. *J. Mater. Sci. Mater. Electron.* **2019**, *30*, 16156–16173. [CrossRef]

58. Bibi, S.; Ahmad, A.; Anjum, M.A.R.; Haleem, A.; Siddiq, M.; Shah, S.S.; Kahtani, A.A. Photocatalytic degradation of malachite green and methylene blue over reduced graphene oxide (rGO) based metal oxides (rGO-Fe_3O_4/TiO_2) nanocomposite under UV-visible light irradiation. *J. Environ. Chem. Eng.* **2021**, *9*, 105580. [CrossRef]

59. Weldegebrieal, G.K.; Sibhatu, A.K. Photocatalytic activity of biosynthesized α-Fe_2O_3 nanoparticles for the degradation of methylene blue and methyl orange dyes. *Optik* **2021**, *241*, 167226. [CrossRef]

60. Song, S.; Hao, C.; Zhang, X.; Zhang, Q.; Sun, R. Sonocatalytic degradation of methyl orange in aqueous solution using Fe-doped TiO_2 nanoparticles under mechanical agitation. *Open Chem.* **2018**, *16*, 1283–1296. [CrossRef]

61. Mohamed Isa, E.D.; Che Jusoh, N.W.; Hazan, R.; Shameli, K. Photocatalytic degradation of methyl orange using pullulan-mediated porous zinc oxide microflowers. *Environ. Sci. Pollut. Res.* **2021**, *28*, 5774–5785. [CrossRef] [PubMed]

62. Djebli, A.; Boudjemaa, A.; Bendjeffal, H.; Mamine, H.; Metidji, T.; Bekakria, H.; Bouhedja, Y. Photocatalytic degradation of methyl orange using Zn@[Fe(CN)$_5$NO] complex under sunlight irradiation. *Inorg. Nano-Met. Chem.* **2020**, *50*, 1115–1122. [CrossRef]

63. Isa, E.D.M.; Shameli, K.; Jusoh, N.W.C.; Hazan, R. Rapid photodecolorization of methyl orange and rhodamine B using zinc oxide nanoparticles mediated by pullulan at different calcination conditions. *J. Nanostructure Chem.* **2021**, *11*, 187–202. [CrossRef]

64. Mallikarjunaswamy, C.; Lakshmi Ranganatha, V.; Ramu, R.; Udayabhanu; Nagaraju, G. Facile microwave-assisted green synthesis of ZnO nanoparticles: Application to photodegradation, antibacterial and antioxidant. *J. Mater. Sci. Mater. Electron.* **2020**, *31*, 1004–1021. [CrossRef]